Geometry of the magma chamber beneath the Damavand volcano (N Iran) from a joint study of gravity and magnetic data

Vahid E. Ardestani [a, b], Naeim Mousavi [c, a *], Mohammad Tatar [c]

[a] Institute of Geophysics, University of Tehran, Tehran, Iran.
[b] Center of excellence in survey engineering and disaster management, Tehran, Iran.
[c] International Institute of Earthquake Engineering and Seismology, Tehran, Iran.

ABSTRACT

Imaging the intra-sediment magma chamber in the Damavand region, northern Iran, is beyond the resolution of the local seismic observations. Gravity anomalies can precisely image the lateral extension of magma reservoir. In order to provide vertical extension of the magma chamber, we apply the inversion of magnetic data with a higher sensitivity to shallow structure in comparison to the gravity data. More importantly, the knowledge of the magma chamber's density allows the prediction of its mechanical behaviour, including the potential of eruption. As Damavand is estimated to be an active volcano, it is important to revisit the physical properties of the magma chamber to be able to evaluate the potential of eruption. Here, we apply the sparse norm inversion of the Bouguer gravity anomaly and magnetic data to model the uppermost crust beneath the Damavand volcano. The qualitative analysis of the Bouguer anomaly shows that the power of the spectrum remains almost unchanged by upward continuation using heights greater than 4 km. Thus, we conclude that the 4-km upward continued Bouguer anomaly represents the regional gravitational effects free from very shallow effects. The inversion of the magnetic anomaly, interestingly, shows a susceptibility structure, with susceptibility contrast of up to ~ +0.025 SI, in the same place as the density anomaly. This study proposes a 10-km wide magma chamber beneath Damavand from depth ~3 km to depth ~12 km. The resulting density structure is comparable with the obtained values from derived densities (using the thermodynamic mineral phase equilibrium) based on geochemical data and those from the conversion of seismic velocity to density. According to the geochemical data analysis, the lava is andesitic which is categorized among dense crustal rocks (2.8 g/cm³). But our modelling results shows a density contrast of maximum + 0.25 g/cm³ between the magma chamber and the surrounding sedimentary rocks (with a density of 2.45 g/cm³) above 5 km. Therefore, we can conclude that the shallow magma chamber, composed of dense andesite, is relatively warm and probably not completely consolidated. The high temperature of the magma chamber appears to be neutralized by the impact of the high density of andesite (naturally dense rocks) to result in a moderate negative anomaly in tomography (i.e., $\Delta Vs = \sim -2$ %). The magma chamber's temperature might exceed 750-800 ºC which is still beyond the solidus-liquid transition temperature of 1100 ºC. Therefore, we can conclude that the magma is no liquid and is partially consolidated.

Keywords: Damavand volcano, Magma chamber, Bouguer anomalies, Magnetic data, Sparse norm inversion.

1. Introduction

The currently dormant volcano of Damavand is located in the north of Iran within the Alborz Mountain ranges (Fig. 1). This volcano forms a vast cone with an approximate volume of greater than 400 km³. However, this is a proxy for the assemblage of the magma chamber beneath the Damavand volcano. The location, physical properties, and presence/absence of erupting magma which is still less explored are of great importance as the Damavand volcano activates periodically and there is ca. 7000 years since its last activity.

Multiple problems are present in understanding the geophysics of the Damavand volcano. On the one hand, seismic profiles [2], tomography [3], and magnetic basement [4] show insignificant heterogeneity beneath Damavand. On the other hand, geochemical data suggest that the volcanic cone is composed of andesite [5, 6] which is different from the Quaternary sedimentary deposits in the vicinity of the summit. Local seismic tomography mainly points to consolidated lava represented by a high-velocity zone beneath the summit [7] (Fig. 2). Other tomography

models show a low-velocity zone beneath Damavand [1, 8] (Fig. 2). However, the following are not yet clear: a) the real depth of the magma chamber, b) the density and susceptibility, and c) the temperature of the magma chamber. In general, our knowledge of the physical properties of the magma chamber beneath Damavand is limited. Therefore, it is difficult to conclude the mechanical behaviour of the magma reservoir.

In light of advances in gravity and magnetic modelling and growing methodological developments [9, 10-12, 13], the density and susceptibility structure of the uppermost parts of the crust beneath Damavand in search of the magma chamber will be conducted. Gravity modelling using the same methodology as this study has been conducted previously for a volcanic region [14] which proves the effectiveness of gravity data modelling for studying the volcanic regions. For example, the density contrast between the magma chamber and ambient rock beneath Laguna del Maule (Chile) is of the order of -0.5-0.6 g/cm³ (e.g., [14]). Study of the density and susceptibility structure

* Corresponding author. E-mail address: : moosavi.naeim@gmail.com (N. Mousavi).
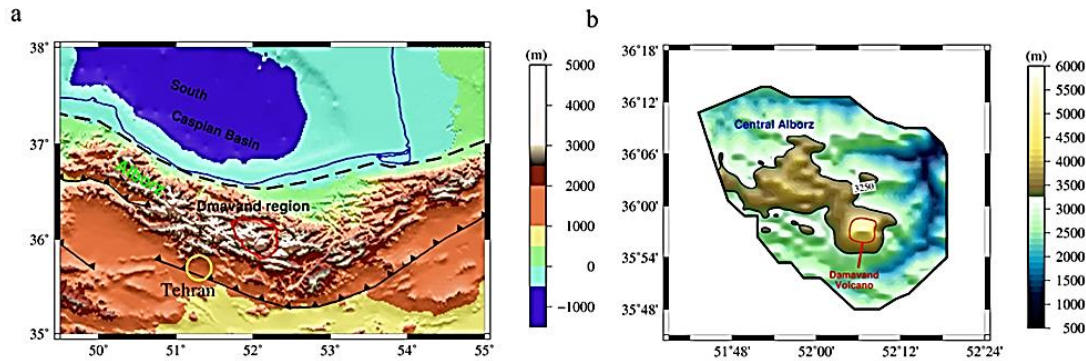
Fig. 1. a) Topography of the region taken from ETOPO1 [38]. Red polygon shows the location of Damavand volcano. B) Zoomed-in map of Damavand volcano including the contour of 3250 m height. Red line shows the area with altitude 4200 m and higher. Yellow circle represents the location of Tehran megacity.
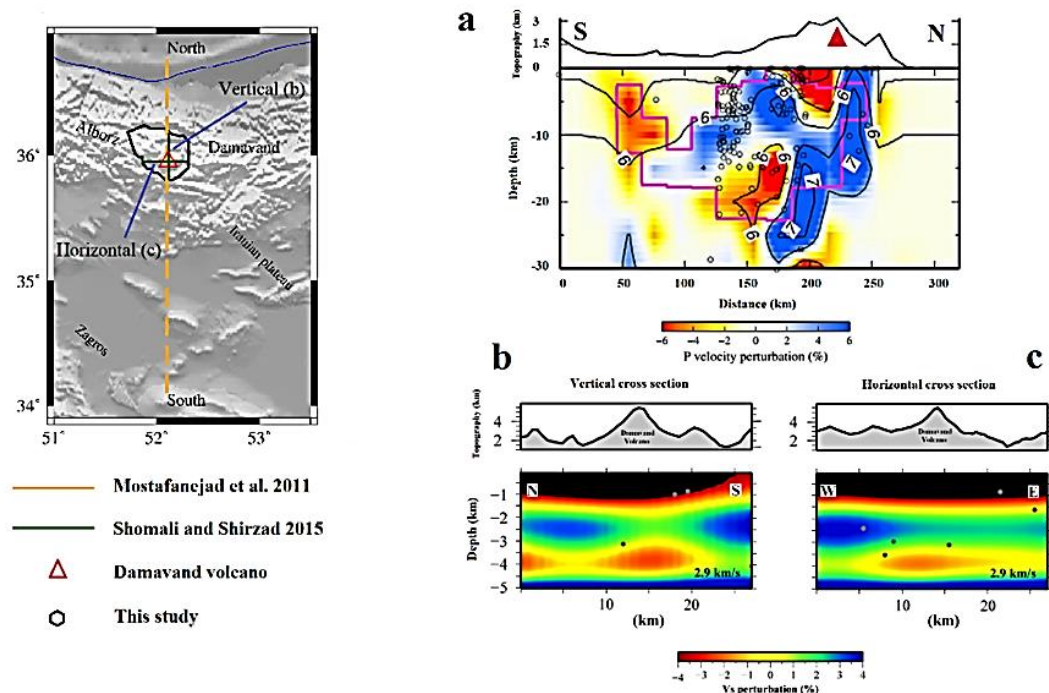
Fig. 2. Summary of seismic information about the shallow structure beneath Damavand volcano. a) locality of previous studies. b) S-N oriented seismic cross section by [7] (their figure 4). (b) S-N oriented cross section and (c) W-E oriented cross section by [1] (their figure 6).

using the gravity and magnetic data is advantageous as the magma chamber is rheologically distinguishable from surrounding sedimentary rocks or granite continental crusts.

This study aims to investigate the magnetic and gravity data of the Damavand volcano using spectral analysis and sparse norm inversion of both data sets. The results for density will be compared to those from the conversion of velocity to density and from the thermochemical modelling results based on geochemical data. The resulted density will be also compared with the laboratorial values for the density of the volcanic rocks, i.e., andesite, to further discuss the temperature of the magma chamber. Moreover, the resulting volume of the magma chamber will be discussed using the tomography models from seismological works. Finally, we will conclude on the eruption potential of the Damavand volcano.

2. Geological and geophysical background

The Damavand volcano presents no eruption activity for the past 7000 years [15]. The geochronological constraints (e.g., [6]) show two episodes when the younger Damavand (~600 kyr) has been formed

above the remnant of the eroded old Damavand (~1.8 Myr). However, there is no difference between the composition of the overlain rocks and the underlying eroded part. The lava that formed the cone is of trachyandesite type, erupted from the summit radially symmetric and cooled to form the composite cone.

Scholars support this belief that the lava is produced in relation to asthenosphere upwelling related to delamination [5, 16]. The erupted rocks have been largely eroded unless the peak of the summit was even higher than its present status [17]. Interestingly, the summit of Damavand is 5670 m (Fig. 1) which counts as the highest peak in the entire Middle East region.

Regarding the tectonics of the area, the Damavand volcano is located within the Alborz ranges constituting an active fold and thrust belts [16]. The Alborz Mountains are uplifted due to the compression forces in the Arabian-Eurasian collision system. In contrast, the South Caspian Basin resists deformation due to its rigid/oceanic affinity [18, 19].

In terms of crustal structure, according to seismic studies, the Moho boundary beneath the Damavand volcano is at depths between 50 and 65 km [20, 2]. A recent integrated geophysical-petrological study constrained by receiver function indicates that the crustal thickness

beneath the Damavand peak is ~55 km [21]. A sedimentary sequence ranges in age from Cambrian to Eocene constitutes the basement beneath the Damavand volcano [15].

3. Input data

The source of the Bouguer gravity anomaly in this study is the global model XGM2019e [22], which is represented by spherical harmonics up to the order of 5399. This degree of spherical harmonics is interpreted as a spatial resolution of 2 minutes (~4 km) (Fig. 3a). Longer wavelength of this data accords with the GOCO06 satellite model, but for short wavelength features, ground-based measurements are used. Combining satellite data with ground-based observations is done using the full normal equations up to the degree and order of 719 (15 min). Comparison the Bouguer anomaly peaks and high topographic contours shows agreement between the important anomalies in the elevation data and Bouguer anomalies (Fig. 3b).

For aeromagnetic data (Fig. 3b), a compiled data by a joint operation of the Geological Survey of Iran (GSI) and the Aeronautical Services Company (USA) is used. This survey has been conducted between 1974 and 1977. The line spacing of this survey is on average 7. 5 km. The flight height has been mainly at altitudes between 500 and 1000 m [23]. The magnetic and topographic anomalies show no notable correlation except at the Damavand summit (Fig. 3).

4. Methodology: Sparse norm inversion

The sparse norm inversion method has been applied for the inversion of Bouguer and magnetic anomalies and consequently modelling the magma chamber. The theory of inversion has been described in [24] and further developed by [9] to be expressed in Python.

The iteratively Re-weighted Least-Squares (IRLS) approach is defined. The IRLS is a well-defined method for inversion and is used by many, such as [25], and [26].

The sparse norm inversion module in SimPEG (0.17.0) inverts the gravity data and enables the recovery of the density contrast [13]. The first step to invert the data is to parametrize the model space which is actually the volume mass from the ground surface to the maximum depth defined by the interpreter. A sophisticated algorithm is used to generate an octree mesh (SimPEG) [27]. Then, the next step is to compute the gravity effect of the model space at the measurement points, or better to say, simulate the gravity effect at these points.

Then, the next step is to compute the gravity effect of the cells in the specified measurement point and the sum of the total effects of all cells is the predicted data at the point. This process is called forward simulation. The forward simulation equation is as follows,

$$F(m) = d_{pred} \tag{1}$$

where d_{pred} is the predicted data and F is the forward equation [e.g., 28] that simulates the measurements.

Computing the simulated data, the data misfit is defined through the L2 norm as follows,

$$\varphi_d(m) = \frac{1}{2}\,|W_d(F(m) - d_{obs})|_2^2 \tag{2}$$

Where F(m) is the simulated data and W_d is a diagonal matrix. The elements of this matrix are equal to:

$$w_{dii} = 1/\epsilon_i \tag{3}$$

where ϵ_i is standard deviation of the *ith* datum. The objective function of the model is expressed using the following norm [29],

$$W_m = [\alpha_s\,I, \alpha_x\,W_x^T\,, \alpha_y W_y^T, \alpha_z W_z^T] \tag{4}$$

where W_m and m_{ref} are the weighting matrix and the reference model (that can be zero), respectively. The matrix W_m is defined as follows,

$$W_m = [\alpha_s\,I, \alpha_x\,W_x^T\,, \alpha_y W_y^T, \alpha_z W_z^T] \tag{5}$$

Here W_m combines smallness and smoothness (first-order) in the x, y, and z directions.

We should consider Eqs. (4) and (5) in addition to the norms and gradients in each direction [30] to have Eq. (6) as follows,

$$\varphi_m(m) = \alpha_s\|W_s R_s(m - m_{ref})\|_2^2 + \alpha_x\|W_x R_x G_x(m - m_{ref})\|_2^2 + \alpha_y\|W_y R_y G_y(m - m_{ref})\|_2^2 + \alpha_z\|W_z R_z G_z(m - m_{ref})\|_2^2 \tag{6}$$

where $\alpha_s, \alpha_x, \alpha_y, and\ \alpha_z$ are the parameters to define the weight of each term, $R_s, R_x, R_y,$ and R_z define the norms, such as [2, 2, 2, 2] (for smooth) or [0, 2, 2, 2] (for sparse norms), and G_x, G_y, G_z define the gradients in the x, y, and z directions.

$$\varphi_m(m) = \alpha_s\|W_s R_s(m - m_{ref})\|_2^2 + \alpha_x\|W_x R_x G_x(m - m_{ref})\|_2^2 + \alpha_y\|W_y R_y G_y(m - m_{ref})\|_2^2 + \alpha_z\|W_z R_z G_z(m - m_{ref})\|_2^2 \tag{6}$$

where $\alpha_s, \alpha_x, \alpha_y, and\ \alpha_z$ are the parameters to define the weight of each term, $R_s, R_x, R_y,$ and R_z define the norms, such as [2, 2, 2, 2] (for smooth) or [0, 2, 2, 2] (for sparse norms), and G_x, G_y, G_z define the gradients in the x, y, and z directions.

Once we have the data misfit and the model objective functions, the optimization is expressed as follows,

$$\text{minimize m,}\ \ \varphi(m) = \varphi_d(m) + \beta\varphi_m(m) \tag{7}$$

such that $\varphi_d \le \varphi_d^*$ $m_i^L \le m_i \le m_i^H$

where β is trade-off or regularization parameter.
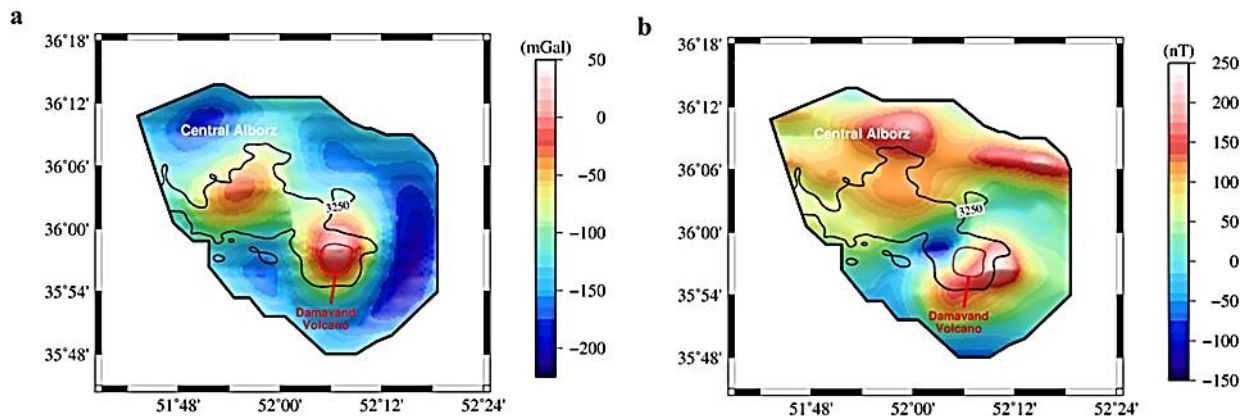
Fig. 3. a) Bouguer gravity anomaly (mGal) for Damavand volcano and surrounding taken from XGM2019e [22]. b) (aero)magnetic data of Damavand volcano provided by Geological Survey of Iran.

Several approaches for the estimation of β are presented in [31], including the Tikhonov curve and cooling techniques. In our sparse inversion, we prefer the cooling strategy [32].

The optimization problem (Eq. (7)) is actually a non-linear problem that can be solved by utilizing the projected Gauss-Newton approach that employs the conjugate gradient solver (SimPEG). In the L2 norm, the objective function Eq. (8) is rewritten as follows [29],

$$\emptyset(m) = \frac{1}{2}\|W_d(F(m) - d_{obs})\|_2^2 + \frac{1}{2}\beta\|W_m(m - m_{ref})\|_2^2 \qquad (8)$$

Our goal is to find m that minimizes Eq. (8), while we assuming β to be fixed.

m^n is the model and δm is the perturbation of the model in an iterative procedure.

$$m^{n+1} = m^n + \delta m \qquad (9)$$

Where computation of δm is described in [9].

$$(J^T W_d^T W_d J + \beta W_m^T W_m)\delta m = J^T W_d^T W_d (d_{obs} - F(m)) - \beta W_m^T W_m (m - m_{ref}) \qquad (10)$$

J is the Jacobian matrix or the sensitivity matrix, reflecting the variation in data,

$$J_{jk} = \frac{\partial F_j}{\partial m_k} \qquad (11)$$

The change in the *kth* model parameter causes the change in the *jth* datum. The iteration (Eq. (8)) continues until a solution is reached which is defined by an acceptable small misfit.

5. Results

Regarding the geometry of the modeled composite representing the magma chamber, this study suggests a maximum depth of ~10 km (gravity modelling, Figs. 4a and 5a) and ~15 km (based on the magnetic modelling; Figs. 4b and 5b) for the magma chamber's vertical extension. The density contrast between the magma chamber and surrounding sedimentary rocks is estimated to be up to 0.25 g/cm³. Our results show the susceptibility contrast of 0.025 SI for the magma chamber compared to the ambient material. [33] showed that the susceptibility of andesite varies between ~0.03 and ~0.12 SI. Our resulting susceptibility is slightly lower than expected (e.g., [33]) which can be explained by the high temperature of the magma chamber as the susceptibility of rocks decreases with an increase in temperature (e.g., [4]). Fig. 4b shows a deep high-susceptibility source in the northern part of the S-N oriented cross section. This might be the deep part of the magma reservoir. However, cares must be taken in interpreting this susceptibility anomaly as neither there is neither any support for this anomaly in other seismic studies nor is the mesh refinement in this corner of the model dense enough to provide reliable susceptibility results by inversion.

For the physical properties of the obtained magma chamber, its density contrast compared to surrounding sedimentary rocks is estimated to be 0.25 g/cm³. Figs. 4a and 5a show that the remaining parts of the model, excluding the magma chamber, are characterized by zero density contrast compared to the reference (2.67 g/cm³). The magnetic anomaly inversion results in the susceptibility contrast of up to 0.025 SI. In the northern part of the profile, there is a deep susceptibility high located at an average depth of 20 km. However, our resolution of meshing is not enough in this region, besides, this anomaly is located at the corner of the grid.

According to our results, the volume of the magma chamber is 500 to 600 km³ which is almost one and half times bigger than the previous estimation. To calculate the volume, we considered the imaged anomaly beneath the Damavand volcano (Figs. 4 and 5). The dimensions of that anomaly are 5 km by 10 km by ~10 km. The magma chamber seems to be located beneath the summit (Figs. 4 and 5). The magnetic data modelling shows that the magma chamber is not exactly vertical and tends toward the SE of the summit, but the gravity data modelling shows the density excess beneath the summit.

The observed, predicted, and normalized misfits of the gravity and magnetic data inversion are demonstrated in Fig. 6 and Fig. 7, respectively. According to our results, the error of the inversion of the gravity data is 8 mGal, and the error of the magnetic data inversion is 15 nT. The statistics of the preferred inverse model are summarized in Table 2.

6. Discussion

6.1. Spectral analysis of the Damavand gravity data

While the magnetic data are very sensitive to shallow structures, the gravity data is sensitive to all of the mass heterogeneities beneath and at the neighbour of the observation point down to the core. In fact, the gravity data have poor vertical resolution but good lateral resolution. Thus, we must assess the energy of the gravity signal to make a proxy of the sensitivity of the observed gravity data at depth (Fig. 3a). This study simultaneously applies the magnetic data to limit the uncertainties in the obtained location of the magma chamber from the gravity data. Figs. 4 and 5 indicate that the source for susceptibility is deeper than density structure obtained from the inversion of the potential field of the Damavand volcano.

Fig. 8 shows the radially averaged power spectrum of the Bouguer anomaly and its upward continuation to heights of 2, 4, and 8 km. Comparing these plots demonstrates that the energy of the original Bouguer anomaly decreases significantly with upward continuation to a height of 2 km. However, there is no significant change in the energy of signal using heights of 4 km and above. This indicates the cut-off heights for upward continuation to distinguish the high frequency effects from the long wavelength contributions by the deep sources.

It is expected to have a deeper source from the inversion of the upward continued gravity data instead of using the original gravity data, as upward continuation makes the gravity anomaly smoothed. We must note that the depth of the inverted density structure does not considerably vary using the original or upward continued Bouguer anomalies. We note that the higher density values from using the original Bouguer anomaly contradict the reference density profile provided by seismic estimates (Fig. 9b). According to our tests, the effects of using upward continued anomaly are reflected in the given density contrast between the anomalous body and the surrounding sedimentary cover. But there is no difference in the depth of the inverted anomalous body. This indicates the insensitivity of the inversion process to the amplitude of the gravity anomaly and the dependency of the inversion only on the width of the gravity high in the location of the magma chamber (~ 10 km width, Fig. 3a).

6.2. The density of the magma chamber (seismic and geochemical studies)

Fig. 9a shows the Vs velocity profiles for a broadband station of the BIN seismic network (IIEEA) which is located ~35 km SW of the Damavand volcano [2]. Both profiles indicate the presence of low-velocity sedimentary cover down to ~5 km depth. The second upper crustal interface observed in the velocity profiles is observable at a depth of ~15 km. The velocity between 5 and 15 km is ~3.5 km/s.

For the conversion of velocity to density, first we need to convert Vs to Vp using the Vp/Vs ratio of 1.73 [2, 8]. Second, the Vp velocity is converted to density using the experimental relation based on global relations between Vp and density ([19] and references therein). Following the above procedure, the density of sedimentary cover is defined to be 2.4 g/cm³, while the density increases to 2.8 g/cm³ between 5 and 15 km. [34] (using the local geochemical data [5] and through a thermochemical modelling procedure where the stable phase mineral is estimated by the minimization of the Gibbs Energy [35]) calculated the density of andesite rocks in the Damavand volcano. Their results also confirm the density of andesite at a depth varying between 5 and 15 km to be 2.8 g/cm³. However, at depths smaller than 5 km, their obtained density does not exceed 2.6 g/cm³.

The densities of the geological formations, including volcanic rocks,

i.e., andesite, are presented in Table (1) [36]. According to our results shown in Fig. 9b, it appears the density of the shallow andesite rocks is <2.6 g/cm³ less than the expected values (2.8 g/cm³, Table 1). To explain this controversy, we suggest that the high temperature of the shallow magma reservoir (andesite rocks) by 300 to 400 ºK than the ambient sedimentary cover.
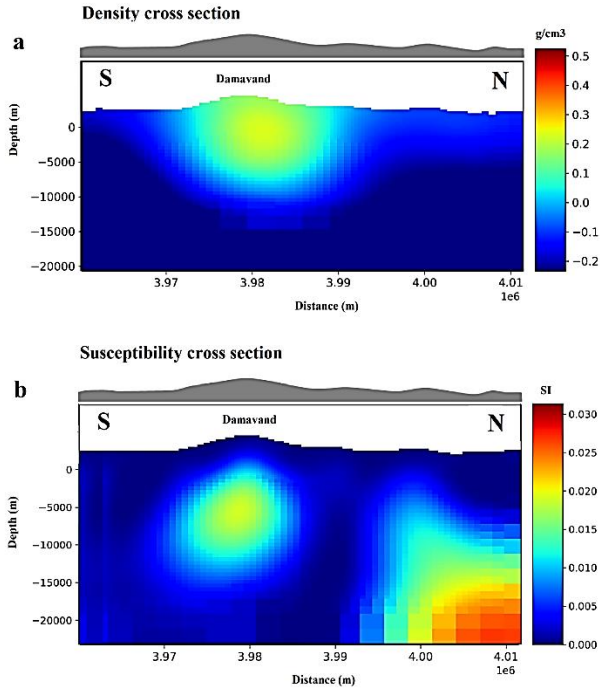

Fig. 4. S-N oriented cross-section of the inversion results for gravity data (a) and magnetic data (b).
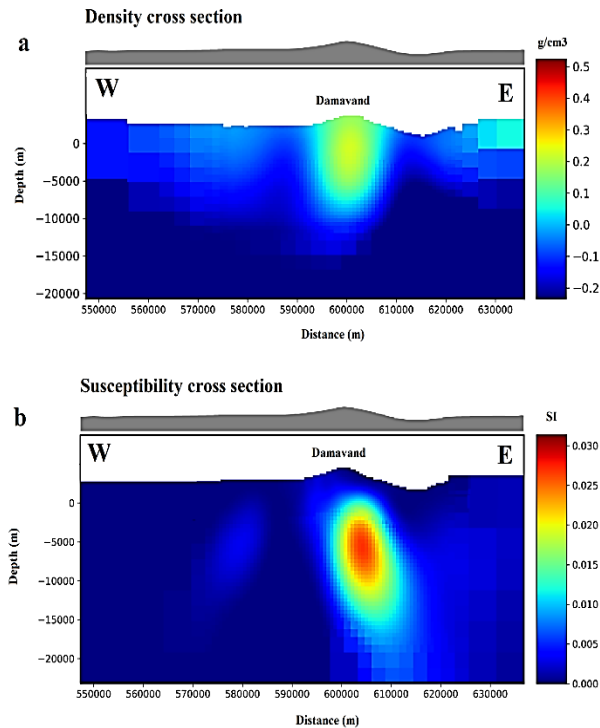

**Fig. 5.** W-E oriented cross-section of the inversion results for gravity data (a) and magnetic data (b).

[37] showed that the temperature of the magma chamber located at a depth of 4-5 km is up to 600 ºC warmer compared to the surrounding region. According to the velocity contrast between the modeled and the observed profiles in Damavand (0.25 km/s, Fig. 9a), we propose that the magma chamber's temperature might be up to 750-800 ºC which is still beyond the solidus-liquid transition temperature of 1100 ºC. Therefore, we can conclude that the andesite assemblage is not fully molten and is partially consolidated.

6.3. Location of magma chamber: potential field vs. tomography

[14] applied a high-density contrast of - 0.5-0.6 g/cm³ between the magma and the surroundings for modelling the magma chamber. The magma chamber in this study is denser than the surrounding, indicating that the lava has been consolidated since the last eruption in ~7 kyr (e.g., [15]). This is because the the gravity anomaly above the Damavand volcano is positive which results in a positive density contrast through an inversion solution for the density model. [7] demonstrated a two-branch cold/ high velocity zone beneath the Damavand summit (Figs. 2 and 10). In contrast, [1] suggested the presence of a moderately warm chamber beneath Damavand indicated by a low-velocity anomaly zone. The sedimentary thickness beneath Damavand (originally for the entire Iran) has been recently provided by [3], showing there is a cover of 8 to 6 km sedimentary cover in this region. This observation is consistent with 1-D and 3-D velocity models obtained from a detailed crustal structure study in the central Alborz [2, 8]. Thus, it appears the magma chamber at shallow depths (<5 km) beneath Damavand is not well imaged by seismic velocity anomaly. Sedimentary cover, as determined by the combined gravity and magnetic modelling [4] shows that the sedimentary cover is 8 km beneath Damavand (Fig. 10). We must note that neither the magnetic [4] nor the seismic [3] basement presents a shallowing in the location of the Damavand volcano, probably, due to the regional scale of those studies. However, these studies provide the regional estimates of sedimentary cover beneath the region and very local upwelling might be neglected by them.

According to our results, the magma chamber is moderately dense, warm, and magnetized, extending between depths of 2 and 12 km. The density anomaly is slightly shallower than the susceptibility anomaly. For reasoning, the shallower parts of the magma chamber might be less magnetized and the deeper part of the magma might be slightly denser than the surrounding. The location and extension of the magma chamber were discrepant in previous local tomography models [1, 7]. Therefore, the results of the present study add important constraints on the physical properties and location of the magma chamber beneath Damavand, unachievable by regional studies.

Fig. 10 represents that the low-velocity zone by [1] (purple box; Fig. 10), is approximately located in the location of our obtained density (black polygon; Fig. 10) and susceptibility (red polygon; Fig. 10) anomalies from this study. However, the thickness of low-velocity anomaly by [1] is much smaller than the thickness of the magma chamber obtained in our study. Therefore, our hypothesis of the high temperature of the magma chamber based on its low density is evidenced by seismic tomography. However, we suspect why seismic tomography (e.g., [1]) does not highlight the presence of the magma chamber. It might be that the high density of andesite (2.8 g/cm³; Table 1) neutralizes the effects of high temperature to be imaged as a very low-velocity zone in tomography. Furthermore, the obtained susceptibility anomaly (susceptibility contrast is equal to up to 0.025 SI) associated with the magma chamber is rather deeper than the density structure, meaning the temperature of the shallow parts (where only density anomaly is located) is higher than optimal to allow the magnetization of shallow rocks. We note that the magnetization and temperature have a linear relationship, meaning the magnetization property degrades once the temperature exceeds a certain value [4]. More reliable data confirm a low-velocity zone located in the south of the Damavand cone, from 2 to 10 km. These results indicate a much deeper low-velocity zone which is located below the Damavand volcano from ~15 km depth to a very deep part at >40km [8, 34]. It seems the latter mentioned low-velocity zone is warmer than the shallow zone.
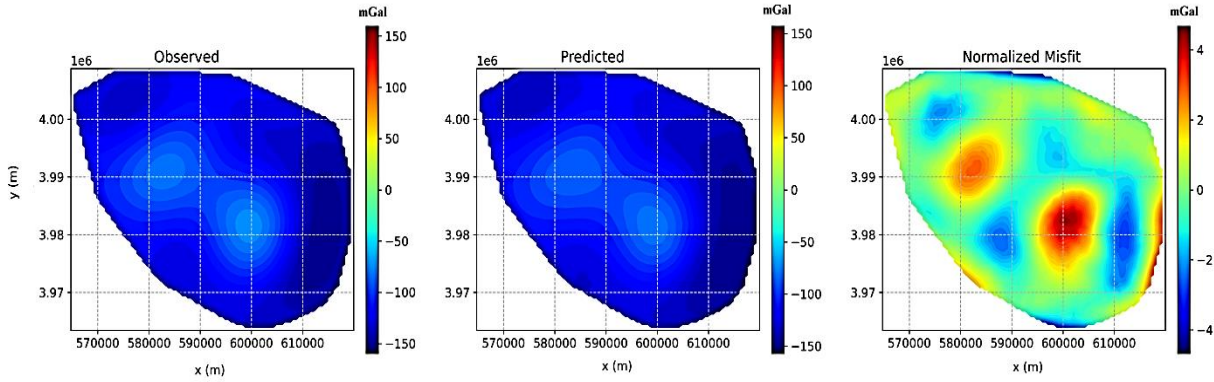
Fig. 6. Gravity inversion and fitting gravity data: a) Observed Bouguer anomalies, b) predicted anomalies, and c) normalized difference between observed and predicted gravity anomalies.
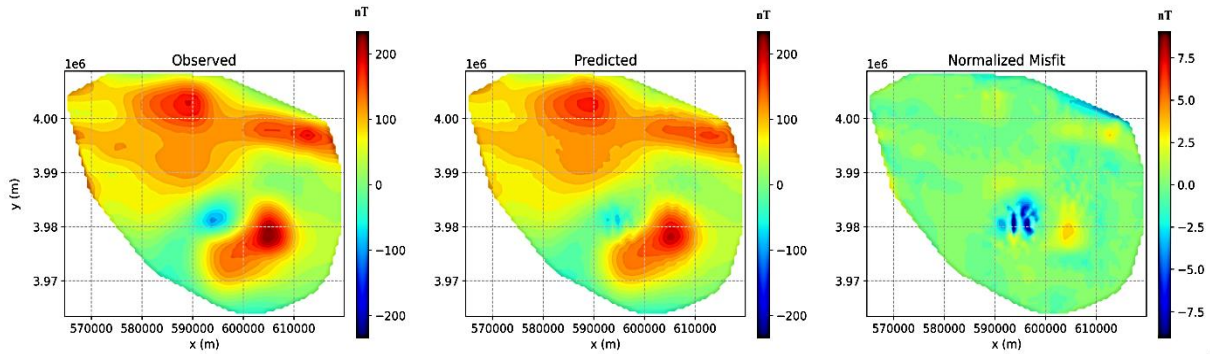

Fig. 7. Magnetic inversion and the quality of fitting magnetic data: a) Observed magnetic anomalies, b) predicted anomalies, and c) normalized difference between observed and predicted magnetic anomalies.
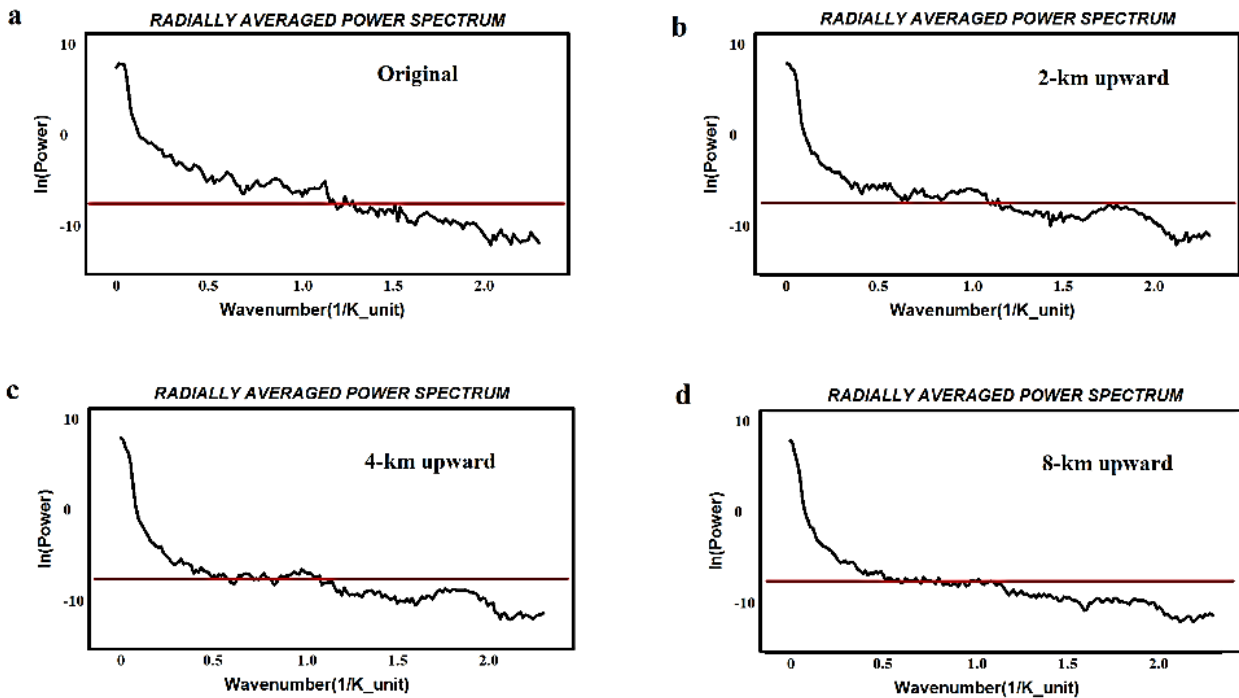

Fig. 8. Radially averaged power spectrum of a) original Bouguer anomaly, b) 2-km upward continued Bouguer anomaly, c) 4-km upward continued Bouguer anomaly, d) 8-km upward continued Bouguer anomaly.

Table 1. The density of different formations taken from [36].

Formation	Average Density (g/cm³)	Formation	Average Density (g/cm³)
Amphibolite (Precambrian)	2.96	Granite (Intrusion bodies)	2.64
Andesite lava (Tertiary)	2.8	Schists (Precambrian)	2.64
Gneiss (Precambrian)	2.8	Limestone (Cretaceous)	2.55
Granodiorite (Intrusion bodies)	2.73	Shale (Triassic)	2.4
Dolomite (Triassic)	2.7	Sandstone (Triassic)	2.35
Tuff (Tertiary)	2.65	Terrace deposits (Quaternary)	~2
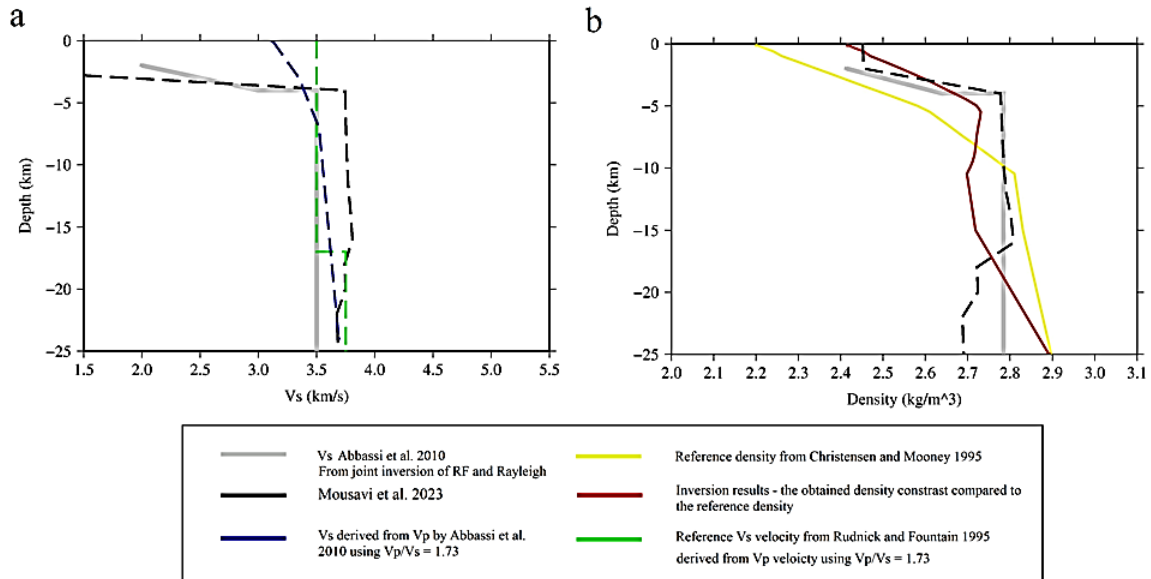
Fig. 9. a) The observed Vs velocity anomaly from [2] using a joint inversion of receiver functions and Rayliegh wave group velocity. Dashed blue line is the converted Vs velocity from Vp by [2] using their suggested Vp/Vs ratio of 1.73. Green line is the Vs derived from Vp by [39]. b) Converted density from velocity shown in section (a). Dashed black lines are density and velocity based on geochemical data and thermodynamic solution of stable minerals [34]. Yellow line is the reference density model from [40]. Our inversion result which is relative density is converted to absolute density to be comparable with other absolute results.
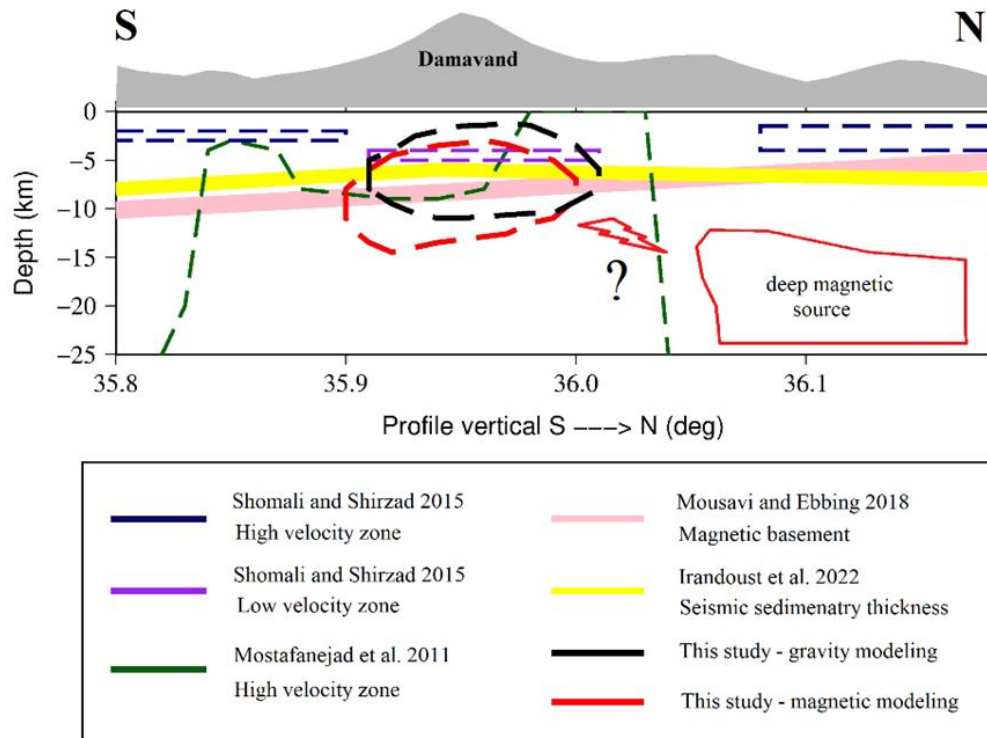
Fig. 10. Cartoon shows the location of modeled anomalies beneath Damavand volcano using gravity and magnetic data. The depth to igneous basement is provided by a combined gravity and magnetic model [4] and a joint analysis of fundamental mode Rayleigh wave group velocities and P-wave receiver functions [3]. The anomalous low and high velocity zone are taken from [7] and [1].

7. Conclusions

The sparse inversion of the Bouguer gravity and magnetic anomaly is used to image the magma chamber beneath the Damavand volcano. This study improves our knowledge of the magma chamber beneath the Damavand volcano. The upwelling magma has been consolidated since the last eruption at ~7 kyr and the magma chamber is clearly distinguishable by its density and susceptibility contrasts compared to the ambient sedimentary rocks. This has not been previously reported due to the lack of geophysical studies using the gravity and magnetic data modelling for the Damavand region. Our results show that moderate density exceeds the magma chamber which is associated with the warmth of the magma chamber. Because we expect a higher density (2.8 g/cm^3) for andesite and the density of andesite is only up to 2.65 g/cm^3 (if we assume a density of 2.45 g/cm^3 for the ambient sedimentary rocks). On the one hand, the presence of low-velocity anomaly (which is interpreted as a warm zone) beneath the Damavand volcano at depths between 4 and 5 km had been previously suggested. On the other hand, the geochemical data indicate the rock type and composition of lava. But this study gives more details on the physical properties and the volume of the magma reservoir.

Furthermore, this study shows the location of the magma chamber beneath Damavand which is disputed in seismic works. More importantly, we can conclude that the warm and dense cone is not necessarily imaged by a low-velocity zone, as temperature and density can neutralize the effects of each other in the final calculation of velocity. Despite the warmth and buoyancy, the density of the mama chamber is still larger than the density of surrounding sedimentary rocks which means it is far to have a quick upward movement of magma. We must note that the primary focus of this study is the estimation of the volume of lava. According to our results, the lava is ca. 400 to 500 km^3 and this amount of lava noticeably creates hazard. In summary, other factors, such as tectonic forces and heating by deep mantle upwelling might enforce the lava, apparently warm enough, to erupt.

Acknowledgment

Appendix: Synthetic tests

A synthetic data is firstly inverted to access the module's capability. The synthetic model is shown in Fig. A1. The assumed contrast density of the model is 0.3 g/cm^3. The gravity effect of the model is shown in Fig. A1. A noise equal to 0.01 of the maximum gravity effect is also considered as the uncertainty of the synthetic data.

The inversion results are demonstrated in cross-sections (Figs. A2a, A2b). An octree mesh is used to parameterize the model space (see text for more detail). The synthetic, predicted, and normalized misfit (divided by uncertainty) data sets are depicted in Figs. A3a, A3b, and A3c, respectively.
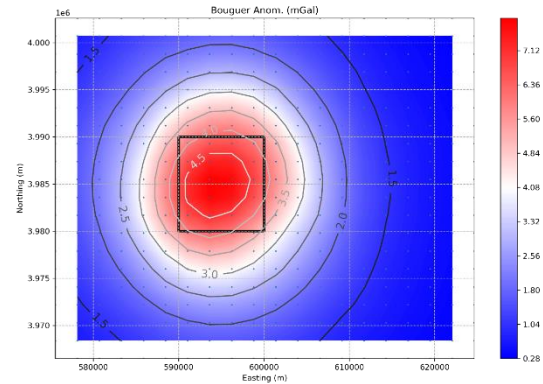

Fig. A1. The Bouguer gravity anomaly (mGal) associated with our synthetic model.
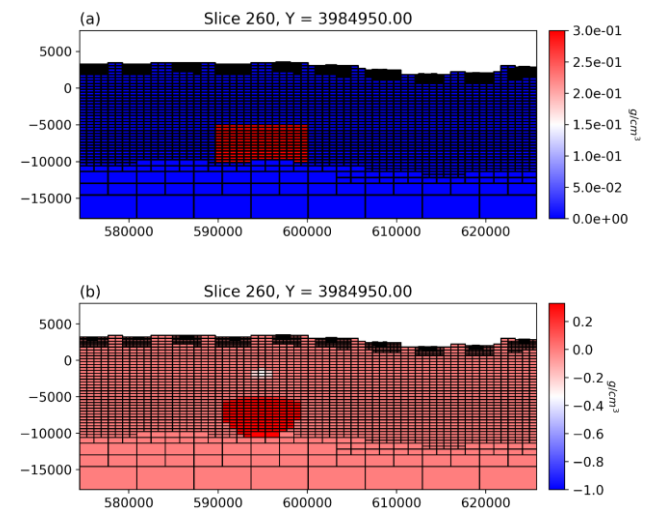

Fig. A2. The cross-section of the inversion results of the synthetic data. a) It shows the synthetic model. b) The predicted model by inversion. The mesh resolution over the target structure, topography, and far from the target structure is shown.
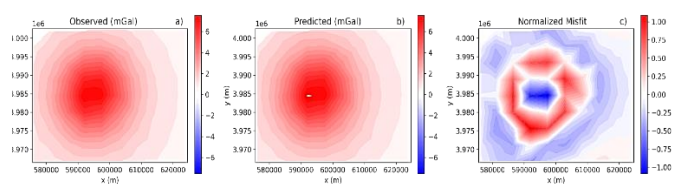

Fig. A3. a) The synthetic gravity data, b) The predicted synthetic gravity data, and c) Normalised difference between the synthetic and predicted data sets.

REFERENCES

[1] Shomali, Z.H., & Shirzad, T., (2015). Crustal structure of Damavand volcano, Iran, from ambient noise and earthquake tomography. Journal of Seismology, 19. doi:10.1007/s10950-014-9458-8

[2] Abbassi, A., Nasrabadi, A., Tatar, M., Yaminifard, F., Abbassi, M. R., Hatzfeld, D., & Priestley, K. (2010). Crustal velocity structure in the southern edge of the Central Alborz (Iran). Journal of Geodynamics, 49, 68–78. doi:10.1016/j.jog.2009.09.044

[3] Irandoust, M.A., Priestley, K., & Sobouti, F. (2022). High-

resolution lithospheric structure of the Zagros collision zone and Iranian Plateau. Journal of Geophysical Research: Solid Earth, 127, e2022JB025009. https://doi.org/10.1029/2022JB025009

[4] Mousavi, N., & Ebbing, J. (2018). Basement characterization and crustal structure beneath the Arabia–Eurasia collision (Iran): a combined gravity and magnetic study. Tectonophysics, 731–732, 155–171. https://doi.org/10.1016/j.tecto.2018.03.018

[5] Mirnejad, H., Hassanzadeh, J., Cousens, B.L., & Taylor, B.E. (2010). Geochemical evidence for deep mantle melting and lithospheric delamination as the origin of the inland Damavand volcanic rocks of northern Iran. Journal of Volcanology and Geothermal Research, 198, 288–296. doi:10.1016/j.jvolgeores.2010.09.014

[6] Mehdizadeh, H., Liotard, J.-M., & Dautria, J.-M. (2002). Geochemical characteristics of an intracontinental shoshonitic association: The example of the Damavand volcano, Iran. Comptes Rendus Geosciences, 334, 111–117.

[7] Mostafanejad, A., Shomali, Z.H., & Mottaghi, A.A., (2011). 3-D velocity structure of Damavand volcano, Iran, from local earthquake tomography. J. Asian Earth Sci., 42,1091–1096. doi:10.1016/j. jseaes.2011.03.011

[8] SoltaniMoghadam, S. (2020). Seismicity and 3D crustal structure of Central Alborz, Iran using local earthquake dataset. International Institute of Earthquake Engineering and Seismology (IIEES), PhD thesis.

[9] Cockett, R., Kang, S., Heagy, L.J., Pidlisecky, A., & Oldenburg, D.W. (2015). SimPEG: an open source framework for simulation and gradient based parameter estimation in geophysical applications. Computer & Geosciences. 85, 142–154. http://dx.doi.org/ 10.1016/j.cageo.2015.09.015

[10] Ardestani, V.E., Fournier, D., & Oldenburg, D. (2021). Gravity and magnetic processing and inversion over the Mahallat geothermal system using open source resources in Python. Pure and Applied Geophysics, 178. doi:10.1007/s00024-021-02763-6

[11] Ardestani, V.E., Fournier, D., & Oldenburg, D. (2022). A localized gravity modeling of the upper crust beneath central Zagros. Pure and Applied Geophysics. doi:10.1007/s00024-022-03065-1

[12] Ardestani, V.E., & Mousavi, N. (2023), The Moho relief beneath the Zagros collision zone through modeling of ground-based gravity data and utilizing open-source resources in Python. Pure and Applied Geophysics. https://doi.org/10.1007/s00024-022-03221-7

[13] Fournier, D., & Oldenburg, D.W. (2019). Inversion using spatially variable mixed ℓp norms. Geophysical Journal International, 218 (1), 268–282. https://doi.org/10.1093/gji/ggz156

[14] Miller, C., Williams-Jones, G., Fournier, D., & Witter, J. (2017). 3D gravity inversion and thermodynamic modelling reveal properties of shallow silicic magma reservoir beneath Laguna del Maule, Chile. Earth and Planetary Science Letters, 459, 14-27. doi:10.1016/j.epsl.2016.11.007

[15] Davidson, J., et al. (2004). The geology of Damavand volcano, Alborz Mountains, northern Iran. GSA Bulletin, 116(1/2), 16–29. doi:10.1130/B25344.1

[16] Shabanian, E., Acocella, V., Gioncada, A., Ghasemi, H., & Bellier, O. (2012). Structural control on volcanism in intraplate post collisional settings: Late Cenozoic to Quaternary examples of Iran and Eastern Turkey. Tectonics, 31, TC3013, doi:10.1029/2011TC003042

[17] Rezaeian, M., Carter, A., Hovius, N., & Allen, M.B. (2012). Cenozoic exhumation history of the Alborz Mountains, Iran: New constraints from low-temperature chronometry. Tectonics, 31, TC2004, doi:10.1029/2011TC002974

[18] Berberian, M. (1983). The southern Caspian: A compressional depression floored by a trapped, modified oceanic crust. Canadian Journal of Earth Sciences, 20, 163–183.

[19] Mousavi, N., & Ardestani, V.E. (2022). The nature of the South Caspian Basin: Oceanic crust formation and lithospheric mantle buoyancy. Physics of the Earth and Planetary Interiors, 325, 106863. doi: 10.1016/j.pepi.2022.106863

[20] Sodoudi, F., Yuan, X., Kind, R., Heit, B., & Sadidkhouy, A. (2009). Evidence for a missing crustal root and a thin lithosphere beneath the Central Alborz by receiver function studies. Geophys. J. Int., 177, 733–742. doi: 10.1111/j.1365-246X.2009.04115.x

[21] Mousavi, N., & Fullea, J. (2020). 3D thermochemical structure of lithospheric mantle beneath the Iranian plateau and surrounding areas from geophysical-petrological modeling. Geophysical Journal International, 222(2), 1295–1315. https://doi.org/10.1093/gji/ggaa262

[22] Zingerle, P., Pail, R., Gruber, T., & Oikonomidou, X. (2019). The experimental gravity field model XGM2019e. GFZ Data Services. https://doi.org/10.5880/ICGEM.2019.007

[23] Yousefi, E., & Friedberg, J.L. (1977). Aeromagnetic map of Iran. Quaderangle F5., Tehran, Geological Survey of Iran.

[24] Li, Y., & Oldenburg, D.W. (1996). 3-D inversion of magnetic data. Geophysics, 61, 394-408.

[25] Green, P.J. (1984). Iteratively reweighted least squares for maximum likelihood estimation and some robust and resistant alternatives. J. R. Statist. Soc., 46(2), 149-192.

[26] Daubechies, I., Devore, R., Fornasier, M. & Gunturk, S. (2009). Iteratively reweighted least squares minimization for sparse recovery. Pure and Applied geophysics, 63(1).

[27] Haber, E., & Heldmann, S. (2007). An octree multi grid method for quast-static Maxvell's equations with highly discontinuous coefficients. J. Comput. Phy., 65, 324-337.

[28] Pluff, D., (1976). Gravity and magnetic fields of polygonal prisms and application to magnetic terrain corrections. Geophysics, 41, 727-41.

[29] Oldenburg, D.W. & Li, Y. (2005). Inversion for applied geophysics: A tutorial, pp. 89–150 (Chapter 5). http://library.seg.org/doi/abs/10.1190/1.9781560801719.ch5

[30] Oldenburg, D.W. & Li, Y. (1994). Subspace linear inverse method. Inverse Problems, 10, 915-935.

[31] Tikhonov, A.V., & Arsenin, V.Y. (1977). Solution of ill-posed problems. John Wiley & Sons, Inc.

[32] Nocedal, J., & Wright, S.J. (1999). Numerical optimization: Springer publishing Co. Inc.

[33] Alatorre-Zamora, M., Campos Enriquez, J., Rosas-Elguera, J., Pena-Garcia, L., Maciel, R., & Fregoso-Becerra, E. (2015). Chapala half-graben structure inferred. A magnetometric study. Geofísica Internacional, 54, 323-342. doi:10.22201/igeof.00167169p.2015.54.4.1699

[34] Mousavi, N., Tatar, M., Shafaii Moghadam, H., & Griffin, W.L. (2023). The crust and upper mantle compositional structure beneath Damavand volcano: Mechanical characteristics and magma storage from an integrated geophysical-petrological

model. Journal of Volcanology and Geothermal Research, 442, 107913. https://doi.org/10.1016/j.jvolgeores.2023.107913

[35] Connolly, J.A.D. (2005). Computation of phase equilibria by linear programming: a tool for geodynamic modelling and an application to subduction zone decarbonation. Earth and Planetary Science Letters, 236, 524–541.

[36] Telford, W.M., Geldart, L.P. & Sheriff, R.E. (1990). Applied geophysics. 2nd Edition, Cambridge University Press, Cambridge. https://doi.org/10.1017/CBO9781139167932

[37] Federica, R., Alfredo, C., Lorenzo, & Salvatore, L. (2018). Regional thermo-rheological field related to granite emplacement in the upper crust: implications for the Larderello area (Tuscany, Italy). Geodinamica Acta, 30, 225-240. doi:10.1080/09853111.2018.1488912

[38] Amante, C., & Eakins, B.W., (2009). ETOPO1 arc-minute global relief model: procedures, data sources, and analysis. NOAA Technical Memorandum NESDIS NGDC-24, 19 pp.

[39] Rudnick, R.L., & Fountain, D.M. (1995). Nature and composition of the continental crust: a lower crustal perspective. Reviews of Geophysics, 33(3), 267-309.

[40] Christensen, N.I., & Mooney, W.D. (1995). Seismic velocity structure and composition of the continental crust: A global view. Journal of Geophysical Research, 100(B7), 9761-9788.